RSC Advances

PAPER

View Article Online
View Journal | View Issue

Open Access Article. Published on 05 October 2016. Downloaded on 1/21/2026 10:05:56 PM.
This article is licensed under a Creative Commons Attribution-NonCommercial 3.0 Unported Licence.

Cite this: *RSC Adv.*, 2016, **6**, 95342

Flexible humidity sensors composed of graphite-like carbon micro-pinecone arrays†

Tomohiko Nakajima,* Takako Nakamura and Tetsuo Tsuchiya

Received 1st September 2016
Accepted 24th September 2016

DOI: 10.1039/c6ra21902k

www.rsc.org/advances

We have prepared flexible graphite-like carbon humidity sensors at room temperature in air. Self-organized carbon micro-pinecone (CMP) arrays consisting of stacks of very thin nanosheets with thicknesses below 5–10 nm and arranged in a pinecone shape were fabricated by KrF laser irradiation of flexible polyimide sheets containing SiO_2 nanoparticles of approximately 5 nm in diameter. The Raman spectrum of CMP showed two clear bands, at 1350 cm^{-1} (D) and 1598 cm^{-1} (G), indicating a typical graphite-like carbon structure. Temperature simulation of photothermal heating during KrF laser irradiation of the polyimide substrate containing a single SiO_2 nanoparticle suggested that the areas surrounding the SiO_2 nanoparticle experience a much higher photothermal heating effect than other areas, leading to preferential combustion of carbon near the nanoparticles. This modulation of the photothermal heating temperature is likely strongly related to CMP formation. The obtained CMP arrays showed high sensitivity for humidity when decorated with surface noble metal nanoparticles and Pt-decorated CMP in particular showed very good response and high sensitivity.

Introduction

Carbon nanomaterials of various geometric shapes and crystal forms hold promise for diverse applications such as gas sensors, supercapacitors, catalysts and tribological coatings.[1–7] These applications would take advantage of the high tunability of carbon nanomaterial surfaces, and thus there has been significant interest in new approaches to the nanostructuring of carbon nanomaterials into fine nanoparticles,[8] nanosheets containing graphite/graphene,[9,10] single/multi-walled nanotubes,[11,12] nanofibers,[13] and nanoflakes.[14] Applications in electronic devices would benefit greatly from planar nanostructures that can exploit the covalent bonding capabilities of sp^2 hybridized orbitals in graphite-based materials to improve electrical conductivity. Moreover, the identification of new nanostructures is essential for maximizing the properties of new sensing devices by providing platforms amenable to optimum surface modifications.

Various chemical vapor deposition methods have been used to fabricate carbon nanomaterials,[14,15] of which the laser combustion process (LCP) has recently received significant attention because of its flexible applications. The LCP can fabricate carbon nanostructured membranes by the combustion of an organic substrate surface such as a polyimide sheet.[16–19] A self-organized carbon micro-cone (CMC) array consisting of carbon nanoparticles prepared by excimer laser irradiation of polyimide substrates is a well-known example,[16,17] and CO_2 laser irradiation of polyimide sheets can be used to fabricate porous graphene membranes.[18,19] A very important advantage of these LCPs is that patterning of carbon nanomaterial films at room temperature in air is straightforward. This is a significant advantage for the fabrication of carbon nanomaterials for use in devices. Therefore, the discovery of new and varied structural forms of carbon nanomaterials using laser processing is important.

We have studied the effect of the combustion source on the formation of carbon nanostructured membrane formation using excimer laser irradiation at room temperature in air and found that a new carbon micro-pinecone (CMP) array was fabricated by the combustion of polyimide substrates containing very small SiO_2 nanoparticles. The obtained CMP arrays were formed by stacking very thin carbon nanosheets. The CMP array nanostructure showed lower sheet electrical resistance than conventional CMC arrays and good humidity sensing properties when the surface was decorated with noble metal nanoparticles.

Experimental procedures

Commercial Pomiran (Arakawa Chemical Industries; thickness: 38 μm) and Kapton (DuPont; thickness: 50 μm) flexible films were used as polyimide source materials. Pomiran is characterized by SiO_2 nanoparticles approximately 5 nm in diameter that are uniformly dispersed in the resin.[20] Kapton contains no SiO_2 nanoparticles in the resin but the surface is coated with

---

Advanced Coating Technology Research Center, National Institute of Advanced Industrial Science and Technology, Tsukuba Central 5, 1-1-1 Higashi, Tsukuba, Ibaraki 305-8565, Japan. E-mail: t-nakajima@aist.go.jp; Tel: +81-29-861-6368

† Electronic supplementary information (ESI) available. See DOI: 10.1039/c6ra21902k

This journal is © The Royal Society of Chemistry 2016

Open Access Article. Published on 05 October 2016. Downloaded on 1/21/2026 10:05:56 PM.
This article is licensed under a Creative Commons Attribution-NonCommercial 3.0 Unported Licence.

a thin layer of SiO_2 to prevent the films from sticking to each other. Pomiran and Kapton films were irradiated with a KrF laser (Compex 110, Lambda Physik) at a fluence of 50–200 mJ cm^{-2} at room temperature in air. Dispersions of Pt, Pd and Au nanoparticles (10 mM; approximately 5 nm in diameter) (Renaissance Energy Research) were spin-coated at 4000 rpm for 10 s on the laser-irradiated polyimide film surfaces to demonstrate their humidity sensing properties. The metal nanoparticle coating procedure was repeated twice and then the films were dried at 100 °C for 30 min.

The microscopic morphology and elemental composition of the samples were examined by field-emission scanning electron microscopy (FESEM; SU9000, Hitachi) and energy dispersive X-ray spectrometry (EDS; Genesis, Edax). Raman spectra were collected using a laser Raman spectrometer (NRS 7100, Jasco). X-ray photoemission spectroscopy (XPS) was carried out using an Al Kα source. The electrical resistance (R) was measured using a two-probe geometry under various dry and humidified gases using a digital multimeter (DMM4050, Tektronix). The relative humidity (RH) during measurements was monitored using a humidity temperature meter (Model 725, B&K Precision). The monitoring setup is shown in Fig. S1.†

Temperature variations during laser irradiation can be described by the heat diffusion equation simplified to express one-dimensional heat flow:[21–23]

$$\rho C\frac{\partial T}{\partial t} = \kappa\frac{\partial^2 T}{\partial z^2} + \alpha I(z,t)$$

where T is the temperature function at time t and depth z, ρ is the mass density, C is the specific heat capacity, α is the optical absorption coefficient, κ is the thermal conductivity and $I(z,t)$ is the laser power density. Details of this calculation are explained in the ESI.†

Results and discussion

Graphite-like carbon nano-micro sized structures on polyimide sheets

Fig. 1a shows FESEM images of laser-irradiated Pomiran surfaces. The surface begins to carbonize at 50 mJ cm^{-2}; shallow cone-shaped undulations are observed at the surface, but no specific nanostructures are evident. The carbonized surface had a definite self-organized structure similar to that of micro-cone arrays at fluence values above 100 mJ cm^{-2}. The diameter of the base of the arrays was 2–3 μm and the depth of the channels increased with increasing laser fluence. It is noteworthy that the observed micro-cones consisted of stacks (a few micrometers thick) of very thin nanosheets with a thicknesses below 5–10 nm and shaped like a pinecone (Fig. 1b and S2†). We call this self-organized structure a CMP array. CMC array structures have been observed on laser irradiated Kapton polyimide sheets,[16,17] as shown in Fig. 1c. These CMC arrays consist of nanoparticulate carbon of approximately 10 nm in diameter, show no other ordered nanostructure, and have base diameters very similar to that of CMP arrays (2–3 μm). A cross-sectional view of CMP arrays prepared using a KrF laser at a fluence of 200 mJ cm^{-2} shows that the channel depth (cone

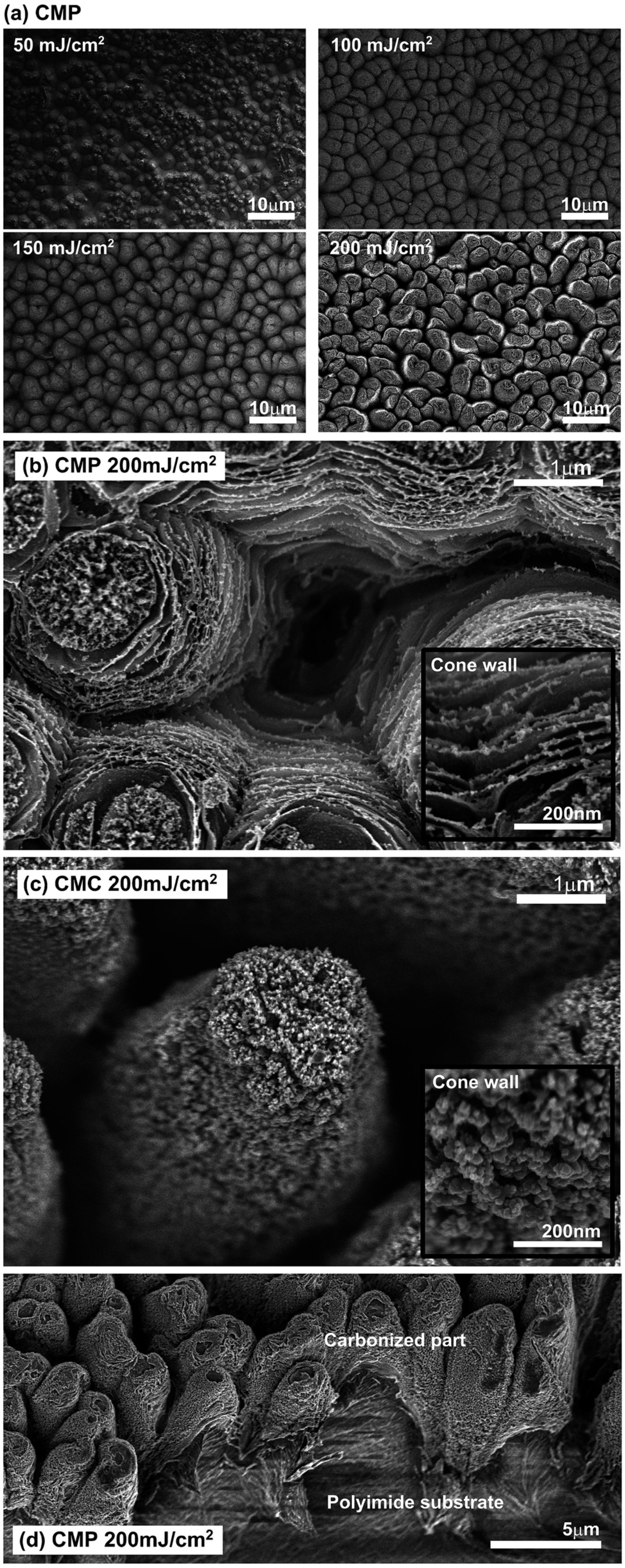

Fig. 1 (a) FESEM images of the CMP arrays prepared by KrF laser irradiation of Pomiran polyimide films at a fluence of 50, 100, 150 or 200 mJ cm^{-2}. Enlarged views of the FESEM images of the CMP arrays are shown in (b) and of the CMC arrays in (c). (d) A cross-sectional FESEM image of the CMP array irradiated at 200 mJ cm^{-2}.

Open Access Article. Published on 05 October 2016. Downloaded on 1/21/2026 10:05:56 PM.
This article is licensed under a Creative Commons Attribution-NonCommercial 3.0 Unported Licence.

height) is approximately 2 μm. Thus, the obtained CMP array structure is very unique among structures obtained by the laser irradiation of carbonized polyimide films.

The Raman spectra of untreated Pomiran and Kapton showed no peaks between 1000–3500 cm^{-1}. In contrast, the CMP and CMC arrays produced by laser irradiation showed characteristic Raman peaks at 1350 cm^{-1} (CMP) and 1362 cm^{-1} (CMC) assigned to the D band and corresponding to defects and disordered structure, and at 1598 cm^{-1} (CMP) and 1612 cm^{-1} (CMC) assigned to the G band and corresponding to bending of the sp^2 bonds in crystalline graphite (Fig. 2a).[24,25] The 2D band at around 2700 cm^{-1} characteristic of graphene[26] was not observed in the present carbonized samples produced by nanosecond pulsed UV laser irradiation. Therefore, the obtained CMP and CMC arrays consisted of graphite-like carbon. The G band peak position of CMP was slightly shifted to lower wavenumber compared to CMC, indicating fewer crystal imperfections in the graphite. In addition, the G band was somewhat larger than the D band in the CMP arrays (the intensity ratio I_D/I_G was 0.924), whereas the G band was somewhat smaller than the D band in the CMC arrays ($I_D/I_G = 1.143$). These relative band intensities further indicate that the graphite-like carbon in the CMP arrays is more crystalline and has fewer defects arising from the graphite-like carbon nanosheets comprising CMP.

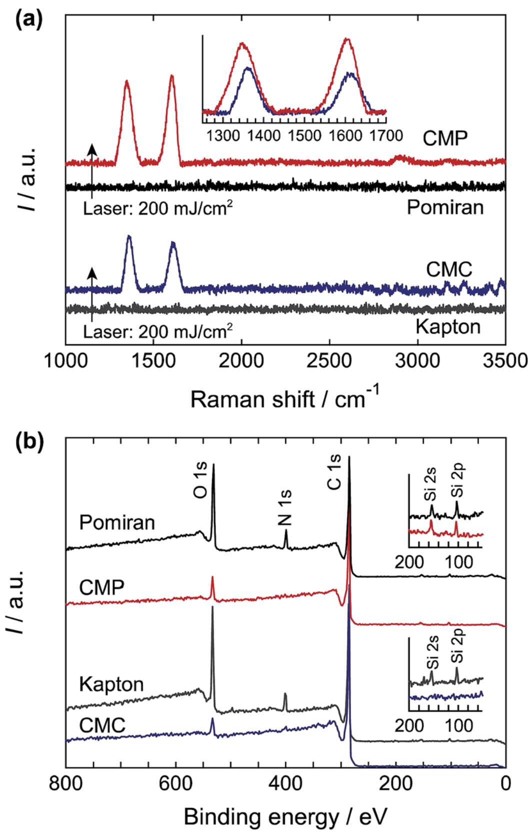

Fig. 2 (a) Raman and (b) XPS spectra of Pomiran and Kapton sheets and the CMP and CMC arrays prepared from each type of polyimide film.

The XPS spectra for Kapton show the Si 2s and 2p peaks prior to laser irradiation, but these peaks are absent in the XPS spectra of the CMC arrays, likely because of laser ablation of the surface SiO_2 thin layer during the pyrolytic reaction with the polyimide surface. In contrast, the XPS peaks due to SiO_2 were present in the spectra of the CMP arrays, indicating that the dispersed SiO_2 nanoparticles remained in the carbonized regions even after laser irradiation (Fig. 2b). Therefore, the differences in the nanostructures of the CMP and CMC arrays result from the original nanoscale compositional distribution of SiO_2 in the polyimide films.

The mechanism by which cone array structures form during laser irradiation of polyimide films without SiO_2 nanoparticles dispersed in the resin has been studied in previous reports.[16,17] In what way does carbonization of polyimide films containing dispersed SiO_2 nanoparticles differ? To qualitatively evaluate the effects of SiO_2 nanoparticles dispersed in the resin, we calculated the temperature distributions in polyimide and graphite during exposure to a single laser pulse; details of the calculation are provided in the ESI.† Fig. 3a shows the temperature map after a single pulse of laser irradiation onto polyimide. The simulated temperature is considerably above 1000 °C for over 6 μs due to the very small thermal conductivity of polyimide (1.2 mW cm^{-1} K^{-1}).[27] This high temperature would cause rapid carbonization after laser irradiation, as seen in the experimental results (the carbonization temperature of polyimide is around 500–600 °C (ref. 28)). After carbonization, the pulsed temperature increase is much lower than is the case for non-irradiated polyimide due to the very high thermal

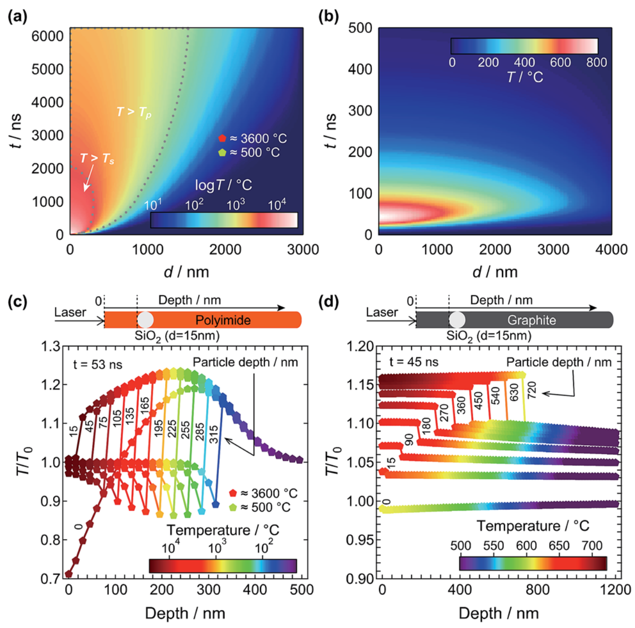

Fig. 3 Simulated temperature mapping as a function of depth and time for (a) polyimide and (b) graphite under KrF laser irradiation at 200 mJ cm^{-2}, and the variation in relative temperature with the depth of the SiO_2 nanoparticle ($d = 15$ nm) in (c) polyimide ($t = 53$ ns) and (d) graphite ($t = 45$ ns). T and T_0 represent the temperatures for models with and without the SiO_2 nanoparticle, respectively.

Open Access Article. Published on 05 October 2016. Downloaded on 1/21/2026 10:05:56 PM.
This article is licensed under a Creative Commons Attribution-NonCommercial 3.0 Unported Licence.

conductivity of graphite (1.12 W $\mathrm{cm^{-1}\,K^{-1}}$).[29] At the initial stage of this process, the significant difference in photothermal heating between the polyimide areas and the carbonized areas results in the formation of cone arrays. Silvain *et al.* speculated that the first carbon nanoparticles produced by laser irradiation could aggregate on the polyimide surface, producing deep channels (cone array formation) as a result of the random distribution of high and low temperature regions.[17]

The surface temperature increased to above 600 °C within several tens of nanoseconds and to a depth of several hundred nanometers. In one model, a single SiO_2 nanoparticle was introduced into the polyimide film at depths ranging from 0–315 nm, whereas the other model contained no SiO_2 nanoparticle. The depth dependence of the relative temperature (T/T_0) between the models with (T_0) and without (T) a SiO_2 nanoparticle 53 ns after the incident pulse is shown in Fig. 3c. The calculated T/T_0 clearly shows a 10–20% increase in temperature behind the SiO_2 nanoparticle at a depth of 350 nm and a decrease of about 5–10% just above the SiO_2 nanoparticle at a depth of approximately 20 nm. This means that polyimide in the vicinity of a SiO_2 nanoparticle is at a higher temperature during laser irradiation than polyimide without SiO_2 nanoparticles. A photothermal simulation was also conducted for graphite as a model of the polyimide substrate surface after carbonization. A single SiO_2 nanoparticle was introduced into the graphite at depths ranging from 0–720 nm; a second model did not contain a SiO_2 nanoparticle. The T/T_0 after 45 ns (Fig. 3d) shows a 5–10% increase in base temperature compared to the model without the SiO_2 nanoparticle, and T/T_0 suddenly increases by 1–7% at the top part of the SiO_2 nanoparticle. The graphite model used in this calculation has very high thermal conductivity and its density (2.26 g $\mathrm{cm^{-3}}$) is the ideal density for graphite.[29] This temperature simulation following carbonization is likely an underestimate since the actual material would have lower thermal conductivity and density. Therefore, these results strongly suggest that the vicinity around the SiO_2 nanoparticles likely undergoes much higher photothermal heating than other areas of the graphite sample.

Fig. 4a shows the EDS spectrum and element maps for the CMP arrays. EDS signals were detected for carbon, Si and O. The element maps revealed Si corresponding to SiO_2 nanoparticles near the edges of graphite-like carbon nanosheets (ring-shaped aggregations) whereas carbon was homogeneously distributed throughout the cones. Based on the thermal simulations and element maps, we suggest that the CMP arrays form by the following mechanism. The cone arrays grow through the formation of micro-domains comprising aggregated carbon nanoparticles that decrease photothermal heating in their vicinity in the molten polyimide sheet.[17] If the polyimide contains SiO_2 nanoparticles, the SiO_2 nanoparticles aggregate along the solid–liquid interface near the base of the cones, resulting in ring-shaped aggregates. At the moment of SiO_2 aggregation, the photothermal heating effect would increase around the aggregated SiO_2 nanoparticles, leading to preferential combustion of carbon nearby the SiO_2 nanoparticles. Carbon located in areas with fewer SiO_2 nanoparticles forms graphite-like carbon nanosheets with residual SiO_2 nanoparticles on the surfaces of the nanosheets. This process is

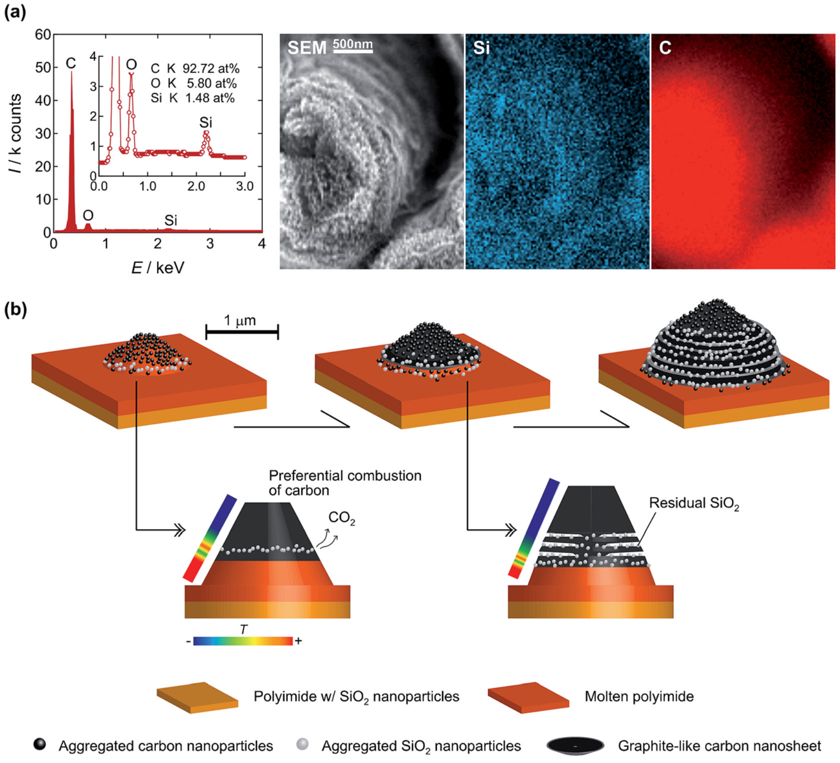

Fig. 4 (a) EDS spectrum and element maps for Si and C in CMP. (b) Schematic illustration of a CMP growth model during pulsed laser irradiation.

Open Access Article. Published on 05 October 2016. Downloaded on 1/21/2026 10:05:56 PM.
This article is licensed under a Creative Commons Attribution-NonCommercial 3.0 Unported Licence.

repeated during pulsed laser irradiation, resulting in the generation of the CMP arrays. It is difficult to obtain direct evidence to support this proposed mechanism because the phase transformations occur on the order of nano- to microseconds; however, the variation in photothermal heating caused by the presence of the SiO_2 nanoparticles and the aggregation of SiO_2 nanoparticles must affect CMP formation. It is very interesting that this new nano/micro-sized carbon structure was realized just by introducing nanomaterials into the carbonized sources and applying simple atmospheric laser irradiation.

Humidity sensing properties of CMP and CMC arrays

We studied the humidity sensing properties of the CMP and CMC arrays. Sensing was enhanced by decorating the surfaces of the CMP and CMC arrays with noble metal (Pt, Pd or Au) nanoparticles. Fig. 5 shows FESEM images of Pt-decorated CMP and CMC (CMP–Pt and CMC–Pt); CMP–Pt and CMC–Pt were prepared by KrF laser irradiation at 200 mJ cm^{-2}, followed by spin-coating of a Pt dispersion. Pt nanoparticles were observed on the surfaces of the carbon nanosheets of CMP–Pt and on the carbon nanoparticles in CMC–Pt. The size of each Pt nanoparticle size was approximately 5–10 nm, similar to the size of the original source Pt nanoparticles.

Fig. 6a and S3† shows a 3 mm square CMP–Pt humidity sensor prepared using KrF laser irradiation at a fluence of 200 mJ cm^{-2} through a photomask and flanked by two silver electrodes fabricated by silver nanoparticle ink deposition. Various CMP and CMC sensors with the same configuration and decorated or not decorated with metal nanoparticles were prepared. Sensors with metal nanoparticles were designated CMP–M and CMC–M (M: Pt, Pd and Au). The prepared sensors were placed in a reaction chamber (Fig. S1†) and the response of R under a flow of dry or humidified N_2 was examined at room temperature. The relative humidity (RH) was concurrently measured using a commercial humidity sensor. CMP had a half sheet resistance (R_S) of 15.7 kΩ sq^{-1} at 0% RH and CMC had an R_S of 31.6 kΩ sq^{-1} at 0% RH; these differences reflect the merit of graphite-like carbon nanosheets for better electrical conductivity (Fig. 6b). Fig. 6c shows the R variations (R/R_0: R_0 represents the R at 0 s) of CMP and CMC as a function of time. The dry N_2 gas flow was changed to 90% RH N_2 from 30 s to 210 s, then was changed back to dry N_2 gas. The R/R_0 of CMP and CMC increased during the humid N_2 gas flow and dropped following the restart of dry N_2 gas flow. This R increase under a humidified atmosphere is due to adsorbed water molecules on the surface of the carbon nanosheets donating electrons to the valence band of carbon, resulting in an increase in electrical resistance due to the lower hole concentration.[30] The sensitivity (S) of the arrays to RH is defined as $S/\% = (\Delta R/R_0)/\Delta(\text{RH}\%) \times 100$. In the absence of surface metal nanoparticles, the sensitivity of CMC was 0.011% and 0.008% for CMP (Fig. 6b). Moreover, the response curves did not follow the reference humidity sensing curve, especially after the restart of dry N_2 gas flow.

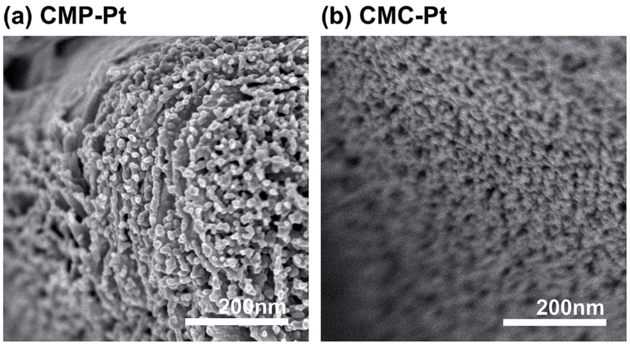

Fig. 5 FESEM images of the cone surface of (a) CMP–Pt and (b) CMC–Pt arrays.

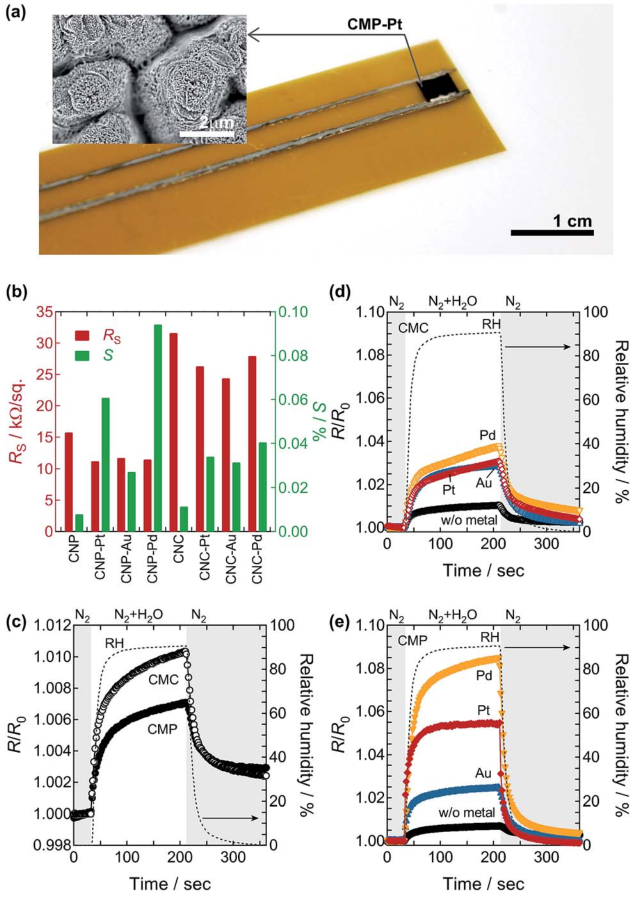

Fig. 6 (a) The fabricated CMP–Pt humidity sensor. (b) The R_S and S of CMP, CMP–M, CMC and CMC–M. The time course of R/R_0 for (c) CMP and CMC, (d) CMC with/without surface metal nanoparticles and (e) CMP with/without surface metal nanoparticles. The dotted line represents the RH curve as monitored using a commercial humidity sensor. In the time course measurements, the gas flow was changed as follows: dry N_2 (0–30 s) – humidified N_2 (30–210 s) – dry N_2 (210–360 s).

In contrast, decoration of the array surface with metal nanoparticles greatly improved S (Fig. 6b). The presence of Pd, Pt or Au nanoparticles on CMC–M increased R/R_0 354% (S = 0.041%), 299% (S = 0.034%) and 276% (S = 0.032%), respectively, compared to CMC without the metal nanoparticles (Fig. 6c). However, the response curves still did not follow the

Open Access Article. Published on 05 October 2016. Downloaded on 1/21/2026 10:05:56 PM.
This article is licensed under a Creative Commons Attribution-NonCommercial 3.0 Unported Licence.

actual humidity variation (Fig. 6d and S4†). Fig. 6e shows the time dependence of R/R_0 for CMP–M. The presence of surface Pd and Pt nanoparticles in particular resulted in improved R/R_0 (S) values. CMP–Pd, CMP–Pt and CMP–Au exhibited significantly increased R/R_0 values of 1195% ($S = 0.094\%$), 772% ($S = 0.061\%$) and 345% ($S = 0.027\%$), respectively, compared to CMP without the corresponding nanoparticles (Fig. 6b and e). In addition, the humidity response of CMP–Pt was in fairly good agreement with the actual humidity variation (Fig. 6e and S5†), while the S value of CMP–Pd was 54% better than that of CMP–Pt.

Fig. 7a and b show the R/R_0 variations for humidified/dry hydrogen and oxygen atmospheres. Flowing humidified H_2/Ar and O_2 over the arrays resulted in an increase in R/R_0, similar to that observed with humidified N_2 flow, whereas R/R_0 was essentially unresponsive to dry gases, indicating that CMP–Pt exhibited a selective response to humidity. The RH dependence of R/R_0 for CMP–Pt at 20 °C is shown in Fig. 7c. The R/R_0 plot exhibited an almost linear increase over a wide range of RH values from 0% to 90%. However, despite the good response and very low noise obtained with the CMP–Pt sensor, two issues should be addressed: (1) the temperature dependence of the sensor and (2) the bending of the sensor. The temperature dependence resulted in an approximately 2% decrease in R in the range between 20–80 °C (Fig. 7d) and the bending test resulted in an R variation of around 1.5–2.0% (Fig. 7e). The temperature dependence of R could be ignored if the S were sufficiently increased. A further increase in S might be achieved by optimally connecting the graphite-like carbon nanosheets within the array (which would also lower the R variation in the bending tests) and optimizing the metal nanoparticles on the nanosheet surface.

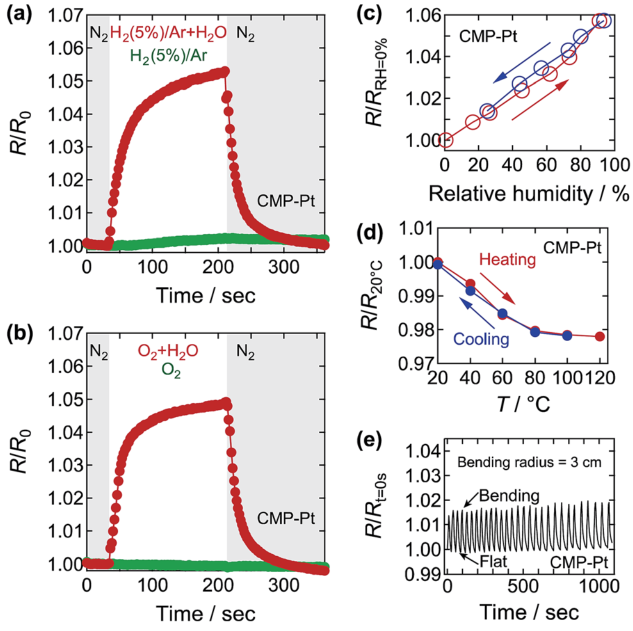

Fig. 7 The time course of R/R_0 for CMP–Pt in (a) dry and humidified H_2/Ar and (b) dry and humidified O_2. The gas flow was changed as follows: (a) dry N_2 (0–30 s) – dry or humidified H_2/Ar (30–210 s) – dry N_2 (210–360 s) and (b) dry N_2 (0–30 s) – dry or humidified O_2 (30–210 s) – dry N_2 (210–360 s). (c) RH ($T = 20$ °C) and (d) temperature (RH = 5%) dependences of the relative R for CMP–Pt. (e) Time course of the relative R at RH = 35% and 20 °C with continuous bending action for CMP–Pt. The bending radius was 3 cm.

Conclusions

We have prepared self-organized CMP arrays from polyimide sheets containing SiO_2 nanoparticles approximately 5 nm in diameter. The arrays were generated by stacks (a few micrometers thick) of very thin nanosheets with thicknesses below 5–10 nm in a pinecone-like structure using KrF laser irradiation at room temperature in air. The Raman spectrum of CMP clearly showed two bands, at 1350 cm^{-1} (D) and 1598 cm^{-1} (G), indicating typical graphite-like carbon formation. Temperature simulation of photothermal heating during KrF laser irradiation of polyimide substrate containing a SiO_2 nanoparticle suggests that the area surrounding the SiO_2 nanoparticle experiences a much higher photothermal heating effect than the other parts of the substrate, leading to preferential combustion of carbon near the nanoparticle. This modulation of the photothermal heating temperature is likely a major determinant of CMP formation. The obtained CMP array showed high sensitivity to humidity when its surface was decorated with noble metal nanoparticles. CMP–Pt in particular showed very good response to high sensitivity. We therefore achieved the fabrication of a flexible humidity sensor by using a very straightforward process at room temperature in air.

Notes and references

1 M. Gautam and A. H. Jayatissa, *Mater. Sci. Eng., C*, 2011, **31**, 1405.
2 M. Penza, R. Rossi, M. Alvisi, D. Suriano and E. Serra, *Thin Solid Films*, 2011, **520**, 959.
3 E. Frackowiak and F. Béguin, *Carbon*, 2001, **39**, 937.
4 M. Sevilla and R. Mokaya, *Energy Environ. Sci.*, 2014, **7**, 1250.
5 Y. Zhu, S. Murali, M. D. Stoller, K. J. Ganesh, W. Cai, P. J. Ferreira, A. Pirkle, R. M. Wallace, K. A. Cychosz, M. Thommes, D. Su, E. A. Stach and R. S. Ruoff, *Science*, 2011, **332**, 1537.
6 L.-W. Zhang, H.-B. Fu and Y.-F. Zhu, *Adv. Funct. Mater.*, 2008, **18**, 2180.
7 A. Erdemir and C. Donnet, *J. Phys. D: Appl. Phys.*, 2006, **39**, R311.
8 S. Y. Lim, W. Shen and Z. Gao, *Chem. Soc. Rev.*, 2015, **44**, 362.
9 T. Hayashi, S. Hirono, M. Tomita and S. Umemura, *Nature*, 1996, **381**, 772.
10 K. S. Novoselov, A. K. Geim, S. V. Morozov, D. Jiang, Y. Zhang, S. V. Dubonos, I. V. Grigorieva and A. A. Firsov, *Science*, 2004, **306**, 666.
11 A. C. Dillon, K. M. Jones, T. A. Bekkedahl, C. H. Kiang, D. S. Bethune and M. J. Heben, *Nature*, 1997, **386**, 377.
12 R. Martel, T. Schmidt, H. R. Shea, T. Hertel and Ph. Avouris, *Appl. Phys. Lett.*, 1998, **73**, 2447.

Open Access Article. Published on 05 October 2016. Downloaded on 1/21/2026 10:05:56 PM.
This article is licensed under a Creative Commons Attribution-NonCommercial 3.0 Unported Licence.

13 A. V. Melechko, V. I. Merkulov, T. E. McKnight, M. A. Guillorn, K. L. Klein, D. H. Lowndes and M. L. Simpson, *J. Appl. Phys.*, 2005, **97**, 041310.

14 N. G. Shang, F. C. K. Au, X. M. Meng, C. S. Lee, I. Bello and S. T. Lee, *Chem. Phys. Lett.*, 2002, **358**, 187.

15 A. M. Cassell, J. A. Raymakers, J. Kong and H. Dai, *J. Phys. Chem. B*, 1999, **103**, 6484.

16 D. J. Krajnovich and J. E. Vázquez, *J. Appl. Phys.*, 1993, **73**, 3001.

17 J.-F. Silvain, H. Niino, S. Ono, S. Nakaoka and A. Yabe, *Appl. Surf. Sci.*, 1999, **141**, 25.

18 J. Lin, Z. Peng, Y. Liu, F. Ruiz-Zepeda, R. Ye, E. L. G. Samuel, M. J. Yacaman, B. I. Yakobson and J. M. Tour, *Nat. Commun.*, 2014, **5**, 5714.

19 Z. Peng, J. Liu, R. Ye, E. L. G. Samuel and J. M. Tour, *ACS Appl. Mater. Interfaces*, 2015, **7**, 3414.

20 http://www.arakawachem.co.jp/en/business/photo/02.html.

21 D. Bäuerle, *Laser Processing and Chemistry*, Springer-Verlag, Berlin, Heidelberg, New York, 2000.

22 T. Nakajima, K. Shinoda and T. Tsuchiya, *Chem. Soc. Rev.*, 2014, **43**, 2027.

23 T. Nakajima, T. Tsuchiya, M. Ichihara, H. Nagai and T. Kumagai, *Appl. Phys. Express*, 2009, **2**, 023001.

24 Y. Liu, M. Zhou, Y. Hu, H. Qian, J. Chen and X. Hu, *CrystEngComm*, 2012, **13**, 4507.

25 L. Marcinauskas, A. Grigonis, P. Valatkevicius and A. Medvid, *Appl. Surf. Sci.*, 2012, **261**, 488.

26 A. C. Ferrari, J. C. Meyer, V. Scardaci, C. Casiraghi, M. Lazzeri, F. Mauri, S. Piscanec, D. Jiang, K. S. Novoselov, S. Roth and A. K. Geim, *Phys. Rev. Lett.*, 2006, **97**, 187401.

27 http://www.dupont.com/content/dam/dupont/products-and-services/membranes-and-films/polyimde-films/documents/DEC-Kapton-summary-of-properties.pdf.

28 J. Su and A. C. Lua, *J. Membr. Sci.*, 2007, **305**, 263.

29 https://www.entegris.com/resources/assets/6205-7329-0513.pdf.

30 J. Chu, X. Peng, P. Feng, Y. Sheng and J. Zhang, *Sens. Actuators, B*, 2013, **178**, 508.